LANGMUIR

pubs.acs.org/Langmuir Article

Silver–Copper Alloy Nanoinks for Ambient Temperature Sintering

Richard Robinson, Virginia Krause, Shan Wang, Shan Yan, Guojun Shang, Justine Gordon, Serena Tycko, and Chuan-Jian Zhong*

Cite This: *Langmuir* 2022, 38, 5633–5644 Read Online

ACCESS | Metrics & More | Article Recommendations | Supporting Information

ABSTRACT: There is an increasing need to reduce the silver content in silver-based inks or pastes and achieve low-temperature sintering for scalable and low-cost production of printed wearable electronics. This need depends on the ability to control the metal composition and the surface properties of the nanoinks. Alloying silver with copper provides a pathway for meeting the need in terms of cost reduction, but little is known about the composition controllability and the low-temperature sintering capability. We report herein a scalable wet chemical synthesis of bimetallic silver–copper alloy nanoinks with room temperature sintering properties. The bimetallic alloy nanoparticles with a controllable composition can be formulated as stable nanoinks. The nanoinks printed on paper substrates are shown to sinter under room temperature. In addition to composition dependence, the results reveal an intriguing dependence of sintering on humidity above the printed nanoink films. These findings are assessed based on theoretical simulation of the sintering processes via surface-mediated sintering and interparticle necking mechanisms in terms of nanoscale adsorption, adhesion and diffusion, and surface free energies. Implications of the findings for room temperature fabrication of wearable sensors are also discussed.

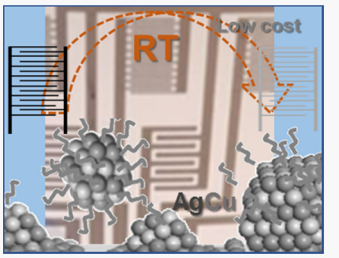

INTRODUCTION

There has been a growing demand for the production and manufacturing of nanoinks or nanopastes for a wide range of applications including medicine, environmental monitoring, sensors, catalysis, and electronics. One of the fastest growing areas of such applications is that of printed electronics for sensors and solar cells. The technology development depends on scalable synthesis of various metal nanoparticles (NPs) with controllable sizes, compositions, and sintering properties. In addition to a high surface area-to-volume ratio, the surface atoms of NPs experience a different chemical reactivity than the bulk counterparts, reflecting transitions from metallic to atomic properties,[1] leading to intriguing mechanical, magnetic, electrical, and biological properties.[1,2] NPs synthesized with noble metals, such as gold, silver, and platinum, exhibit multifunctionality and tunable surface functionalization.[3] Coinage metals such as gold, silver, and copper have a distinct localized surface plasmon resonance (LSPR),[4,5] which has attracted interest in developing advanced sensors and electronics.[6] Silver has been at the forefront of nanoscale research in recent years because of its enhanced surface plasmon resonance. In accordance with other noble metals, silver is known for its stability, conductivity, and facile synthesis. One of the major drawbacks, however, is the high and volatile cost. According to the US 2021 financial report, the market value for silver was $0.81/g, which is much more expensive than other transition metals such as nickel and copper, which had 2021 market values of $0.02/g and $0.01/g, respectively. Silver also fluctuates at a much more drastic monthly level compared to copper, making it more susceptible to market swings. While copper has advantages over silver and other noble metals in terms of cost, it faces serious challenges in stability. Under atmospheric conditions, copper has a high propensity to oxidize, making it more difficult to synthesize copper-based nanoparticles (CuNPs) under ambient conditions.[7] Certain measures can be taken to prevent rapid oxidation, such as the addition of stabilizers or running synthesis under nitrogen and argon.[8,9] These measures, however, can be costly and time consuming, making the overall synthesis process for CuNPs less favorable than that of silver nanoparticles (AgNPs) despite the cost benefit. Alloying the two metals not only addresses the issue of the high cost of silver but also the issue of copper oxidation. In addition, alloying can change the properties from those of the monometallic NP forms.[8] Bimetallic nanoalloys feature a random combination of the metals in the alloy structure, whereas the core–shell structure develops an outer coating of one metal on the other. A key challenge to the synthesis of silver–copper NPs is the ability to control size, composition, phase structure, and oxidation resistance.

Despite significant progress in the synthesis of bimetallic silver–copper NPs,[10−12] the ability to control the bimetallic nanoclusters (NCs) and NPs remains a challenge. Often the presence of NCs makes it difficult to separate NCs from NPs. The process of Ostwald ripening can occur in which larger

Received: January 26, 2022
Revised: April 12, 2022
Published: April 27, 2022

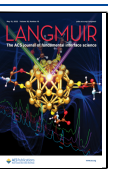

particles grow at the expense of smaller particles. On the other hand, the process of reverse Ostwald ripening occurs when smaller particles break away from the NCs, which can lead to a bimodal distribution of NCs/NPs.[13] Different methods such as wet chemical and physical methods have been demonstrated for the synthesis,[14−18] but most of the methods require organic solvents and high temperature. The NPs synthesized in aqueous solution or low temperatures often suffer from instability due to the propensity of aggregations. For applications of NPs as nanoinks or nanopastes for printed conductive devices, most AgNPs require relatively high temperatures (>70 °C) to sinter, which is problematic for devices involving temperature-sensitive substrates such as paper substrates. There have been limited reports on the ability of near-room temperature sintering for silver-based nanoinks or nanopastes. Some reports showed that Ag NPs and nanowires exhibit room temperature sintering properties in the presence of electrolytic halides.[16,17] For example, AgCu core−shell NPs synthesized under organic conditions were sintered at room temperature utilizing a reducing agent like hydrazine. In other methods, the room temperature sintering involved galvanic displacement and subsequent electrolytic conditions.[18,19] We report herein a new approach to scalable synthesis of silver−copper (AgCu) alloy NPs and nanoinks with room temperature sintering capability. The nanoinks/pastes prepared from the AgCu NPs with a controllable composition are stable and can easily sinter on paper substrates at ambient temperatures without any subsequent chemical treatments, which is promising for fabricating conductive traces or devices for applications in sensors, solar cells, and wearable electronics.

EXPERIMENTAL METHODS

Chemicals. The metal precursors to produce AgCu NPs were all purchased from MilliporeSigma. Silver nitrate ($AgNO_3$, 99.998%), copper(II) nitrate trihydrate ($Cu(NO_3)_2{\bullet}3H_2O$, 99%), and trisodium citrate dihydrate ($Na_3C_6H_5Na_3O_7.2H_2O$, ≥99.0%) were used as the capping agent to prevent aggregation. The reducing agent of sodium borohydride powder ($NaBH_4$, ≥98%) was also required for each synthesis. Hydroxyethyl cellulose was used as an additive to increase viscosity in nanopaste formulations. Each of the chemical precursors was purchased new and handled with care to avoid contamination.

Synthesis. Bimetallic AgCu NPs were synthesized at ambient temperatures using a wet chemical reduction method by controlling the feeding ratios of the metal precursors. To carry out this synthesis under nitrogen, which prevents copper oxidation and nanoparticle aggregation, a Schlenk line was set up for the entirety of precursor additions. This line carried a constant flow of nitrogen through the whole system, which continued for 1 h after all the precursors were added. In a round-bottom flask, 40 mL of deionized water (DI, 18.2 MΩ) was purged with nitrogen for 10 min under stirring at 700 rpm. After purging, 0.100 mL of $Cu(NO_3)_2$ (1 M) was added to water via a micropipette. Next, the capping agent, 0.100 mL of sodium citrate (0.88 M), was added. The purpose of adding this capping agent directly after copper was to help increase colloidal stability and decrease aggregation during synthesis. The next step required the addition of 0.100 mL of $AgNO_3$ (1 M). Lastly, 0.800 mL of reducing agent, $NaBH_4$ (0.25 M), was added slowly in excess to the flask. The formation of the bimetallic NPs was evidenced by the color changes where the solution transitioned from light blue after the addition of metal precursors and capping agent to dark brown upon addition of the reducing agent (Figure S1). Assuming 100% yield, the resulting solution of the NPs (radius = 7.1 nm) contains about 10^{14} NPs/mL. The reducing agent was added lastly to maintain a higher degree of control over nanoparticle production. The as-synthesized NPs were thoroughly washed of the capping agent and centrifuged at 15,000 rpm for 45 min. The colorless supernatant was decanted, and the remaining powder was resuspended in DI water.

Ink/Paste Formulation. Nanoinks were formulated by mixing a solution with 30 wt % NPs, 30 wt % ethylene glycol, 30 wt % DI water, and 10 wt % ethanol. The mixture was ultrasonicated in an ice bath for 3 cycles of 15 min. The mixture was then stored at 5 °C for later use. Nanopastes were formulated with 30 wt % NPs, 50 wt % of 5% hydroxyethyl $cellulose_{(aq)}$, and 20 wt % ethylene glycol. The mixture was then ultrasonicated for a cycle of 1 h 15 min in an ice water bath, which was stored at 5 °C for later use.

Instrumentation and Measurements. *Ultraviolet−Visible (UV−vis) Spectroscopy.* UV−vis spectroscopy was utilized to identify the SPR for various compositions of AgCu NPs. An Agilent 8543 UV−vis spectrometer with a range of 200−1100 nm and both tungsten and deuterium lamps were used for analysis. A blank of DI water in a disposable cuvette was run before any sample measurement, and a base scan of 150.00 μL of synthesized solution sample was typically analyzed for each solution. Pure silver samples were analyzed with less than 125.00 μL, and $Ag_{23}Cu_{77}$ samples were analyzed with 250.00 μL.

Inductively Coupled Plasma−Optical Emission Spectroscopy (ICP−OES). ICP−OES was used to determine the elemental composition of the AgCu NPs. The samples were prepared with concentrated nitric acid and left to decompose the solutions for 1 h. After decomposition, the remaining nitric acid was boiled off. The metallic components left in the solution after burning all the acid were mixed with DI water and left to cool for another 1 h. Then, 10 mL of the metal−water mixture was pipetted and analyzed with the ICP−OES instrument.

Transmission Electron Microscopy (TEM). TEM was used to capture images of the NP surfaces for identification of NP size, shape, and structure. A JEOL JEM-ARM200F instrument was used and operated at 200 kV.

X-ray Diffraction (XRD). A Philips X'Pert PW 3040 MPD X-ray diffractometer was used to collect XRD data for various compositions of AgCu NPs. The NPs were cleaned and stripped of the capping agent, then concentrated, and dispensed onto a quartz crystal.

Dynamic Light Scattering (DLS). The samples were diluted in a 1:2 ratio with DI water. DLS measurements were recorded using a Zetasizer Ultra (Malvern Panalytical Ltd., UK), fitted with a 10 mW 632.8 nm laser, with measurement performed using a side scatter with a 90° scattering angle.

Zeta Potential Measurements. Samples were diluted in a 1:2 ratio with DI water. All measurements were recorded using a Zetasizer Ultra (Malvern Panalytical Ltd., UK), fitted with a 10 mW 632.8 nm laser, with measurement performed using a side scatter with a 90° scattering angle.

Electrical Resistance Measurements. Measurements of resistances were recorded using a BK Precision 393 digital multimeter with an IR USB connection for two-probe measurements. Sheet resistance was measured using a four-probe digital multimeter (Suzhou Jingge Electronic M-3).

RESULTS AND DISCUSSION

Composition, Morphology, and Structures of AgCu NPs. *Bimetallic Composition.* AgCu NPs were synthesized via chemical reduction in aqueous solutions. Briefly, $Cu(NO_3)_2$ was added first to the solution and then capped with sodium citrate, which produced a coordination complex. The formation of this coordination complex caused a color change from clear to blue (see Supporting Information). The capping agent also acted as a weak reducing agent to Cu^{2+}, which reduced the surface energy of Cu^{2+} ions and prevented aggregation. Then, $AgNO_3$ was added directly after the capping agent, where it bound to the capped Cu−ligand complex. No color change was observed at this step. The chemical reducing agent, $NaBH_4$, was then added in excess to the solution. This method produced a solution of AgCu NPs

https://doi.org/10.1021/acs.langmuir.2c00221
Langmuir 2022, 38, 5633−5644

with excellent suspension, showing no indication of aggregation.

The bimetallic composition of the AgCu NPs is controlled by the feeding ratio of the metal precursors in terms of the moles of $AgNO_3$ and $Cu(NO_3)_2$ in the solution. The NP compositions were determined by ICP−OES. The molar feed percentages of Ag and Cu in the solution were compared to the Ag and Cu composition in the NPs that was determined by ICP−OES. As shown by the plot of Ag% in the NPs versus Ag % in the solution in Figure 1, the slope of 1.05 is clearly

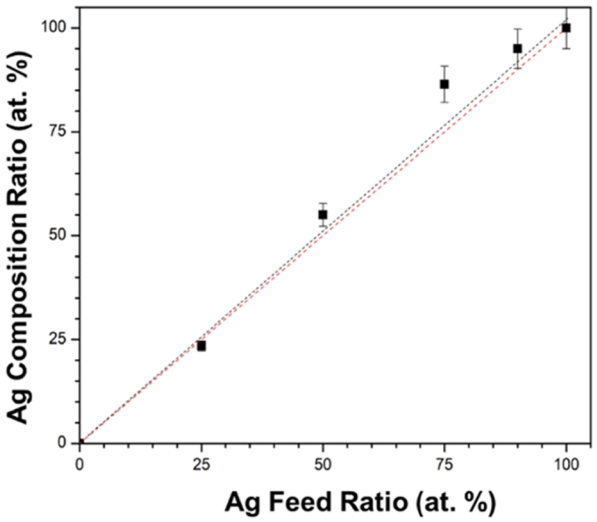

Figure 1. Correlation between the molar feed ratio of Ag and ICP−OES-determined Ag composition in AgCu NPs (linear regression: Ag % (in NPs) = 1.05 Ag% (feeding) + 0.41) (the red dashed line represents an ideal 1:1 relationship).

indicative of a 1-to-1 relationship. Since the intercept of 0.4 is close to 0, the slope suggests that the Ag% in the NPs is slightly higher than that in the solution, especially at higher Ag% concentrations. This finding suggests a slightly higher favorability of Ag over Cu in the bimetallic AgCu NPs during the synthesis. This subtle difference can be explained by the difference of the redox potentials of Ag^+ (0.800 V) and Cu^{2+} (0.342 V). The reduction potential for BH^{4-} is −1.240 V in basic solution and −0.481 V in acidic solution. This implies that the reduction of Ag^+ occurs more favorably than that of Cu^{2+}, especially when in the reaction vessel the concentration of Ag^+ is greater than or equal to that of Cu^{2+}. At reaction concentrations where Ag^+ is less than Cu^{2+}, this difference diminishes with the decrease of the silver ion concentration as expected by the Nernst equation.

Overall, the experimentally determined composition established a 1:1 relationship between the NP and feeding compositions, demonstrating that the synthesis itself can be well controlled by the feeding molar ratios of the two metal precursors. Since the NPs were thoroughly washed, by which any presence of monometallic Cu NPs would not have survived due to the propensity of oxidation of Cu back to Cu^{2+} ions, the observed 1:1 relationship in Figure 1 serves as a clear piece of evidence for the presence of Cu in the as-synthesized AgCu NPs. This synthesis is also scalable as demonstrated by the result from an 8× scale-up synthesis of $Ag_{75}Cu_{25}$ NPs (Figure S2). Optimization of the synthesis parameters is still needed for the scale-up synthesis with the other compositions.

Size and Morphology. To determine the nanoparticle morphology, size, and surface properties, TEM, DLS, and zeta potential measurements were performed for the NPs synthesized with a series of compositions. Figure 2 shows a representative set of TEM images for the as-synthesized AgCu NPs. Ag NPs synthesized under the same conditions were included for comparison (Figure 2a), which features an average radius of 7.4 ± 2.4 nm (Figure 2e). The pure AgNPs also showed very little aggregation. In contrast, AgCu NPs showed the presence of similar-sized NPs and a clear increase in particle size due to the aggregation of the neighboring particles. For example, $Ag_{86}Cu_{14}$ NPs showed NPs with an average radius of 8.2 ± 3.8 nm and larger NPs reflecting the aggregation of the neighboring particles (Figure 2b,f). This

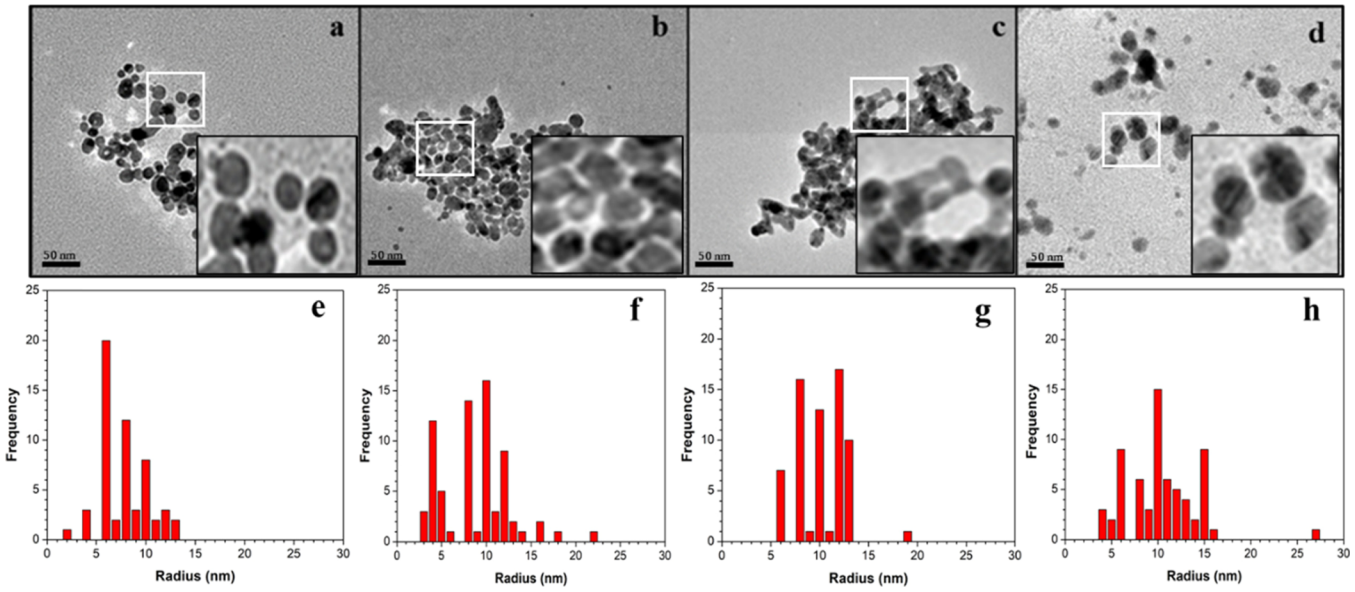

Figure 2. TEM images of AgCu NPs for (a) Ag, (b) $Ag_{86}Cu_{14}$, (c) $Ag_{55}Cu_{45}$, and (d) $Ag_{23}Cu_{77}$ NPs (scale bar: 50 nm) with insets of magnified areas and the corresponding particle size distributions (e−h).

https://doi.org/10.1021/acs.langmuir.2c00221
Langmuir 2022, 38, 5633−5644

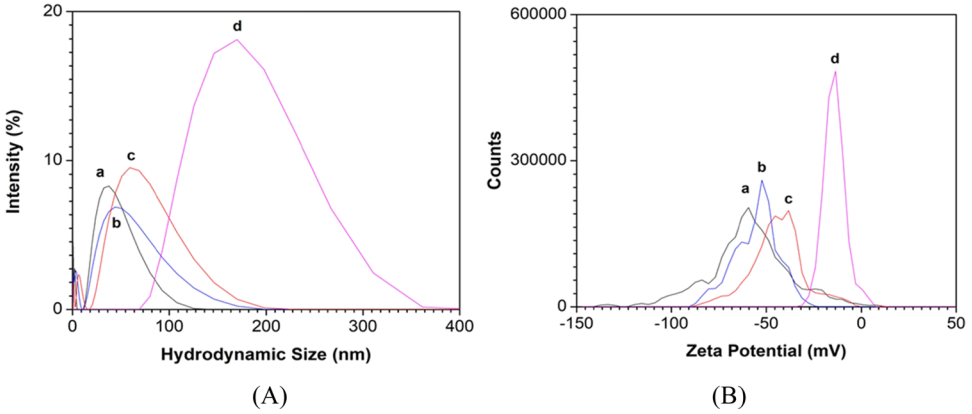

Figure 3. (A) DLS plots of AgCu NPs with different compositions. (B) Zeta potential plots of the same set of AgCu NPs. $Ag_{95}Cu_{05}$ (a, black), $Ag_{86}Cu_{14}$ (b, blue), $Ag_{55}Cu_{45}$ (c, red), and $Ag_{23}Cu_{77}$ (d, purple).

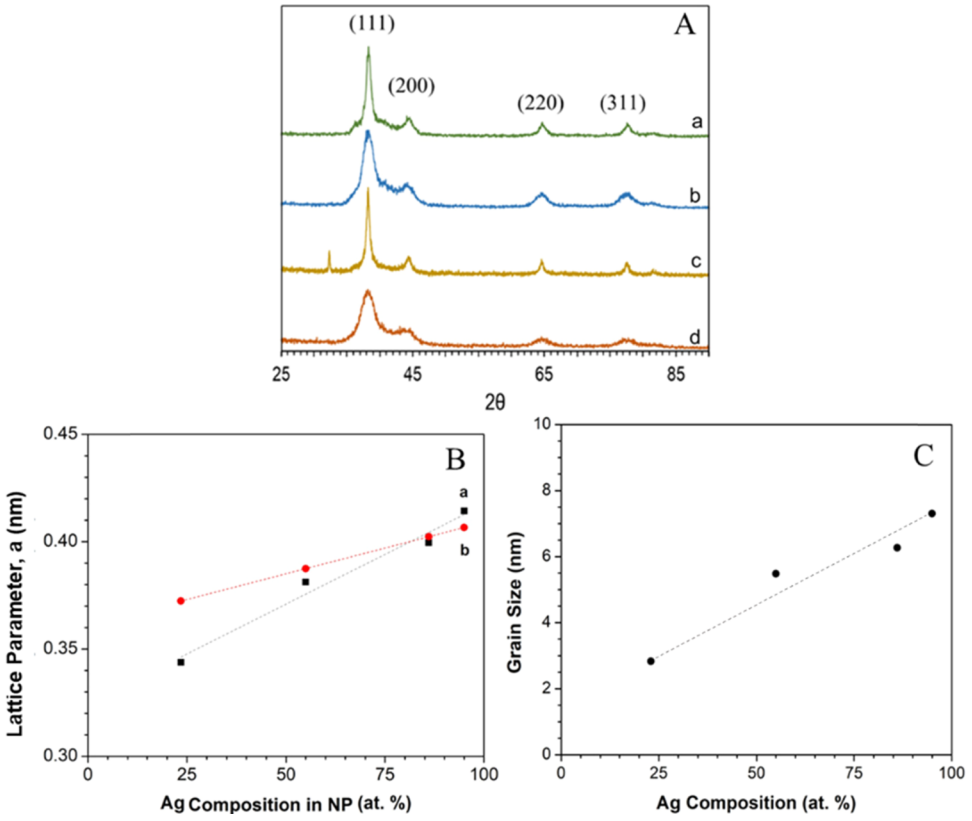

Figure 4. (A) XRD patterns for AgCu NPs with different compositions: (a) $Ag_{95}Cu_5$, (b) $Ag_{86}Cu_{14}$, (c) $Ag_{55}Cu_{45}$, and (d) $Ag_{23}Cu_{77}$ (note that the peak at $2\theta = 29°$ in (c) was due to the sample holder). (B) Plot of lattice parameter based on XRD characterization for AgCu NPs (a, red) in comparison with calculated values from Vegard's law (b, black). (C) Plot of average grain size based on XRD data of AgCu NPs versus the composition.

tendency of aggregation clearly increased as the Cu% is increased in the NPs. This is evidenced by the data for $Ag_{55}Cu_{45}$ NPs (Figure 2c,g), which showed NPs with an average radius of 9.9 ± 2.5 nm and NP networks due to a much higher degree of aggregation than the samples with higher Ag compositions. In this study, we focused on the nanoink/paste formulation for printing and room temperature sintering. As such, the TEM characterization focused on the general morphologies of the NPs. The details such as defects, crystal twins, or stacking faults will be studied in future work.

Considering that the as-synthesized bimetallic NPs are very stable in solution (no indication of aggregation/precipitation for months for NPs with 50% Ag), the different degrees of aggregation for bimetallic NPs revealed by TEM are believed to reflect the difference of sintering on the TEM grid under the ambient conditions between the bimetallic NPs and the pure silver NPs. It is evident that the bimetallic NPs exhibit a greater tendency of aggregation under room temperature on the surface of the carbon film of the TEM grid. The increases in particle size for the bimetallic NPs reflect a surface-mediated Ostwald ripening process, where the larger AgCu NPs were formed at the expense of smaller particles on the surface of the carbon film substrate. Apparently, the surface-mediated Ostwald ripening process is greatly favored as the Cu% is

https://doi.org/10.1021/acs.langmuir.2c00221
Langmuir 2022, 38, 5633−5644

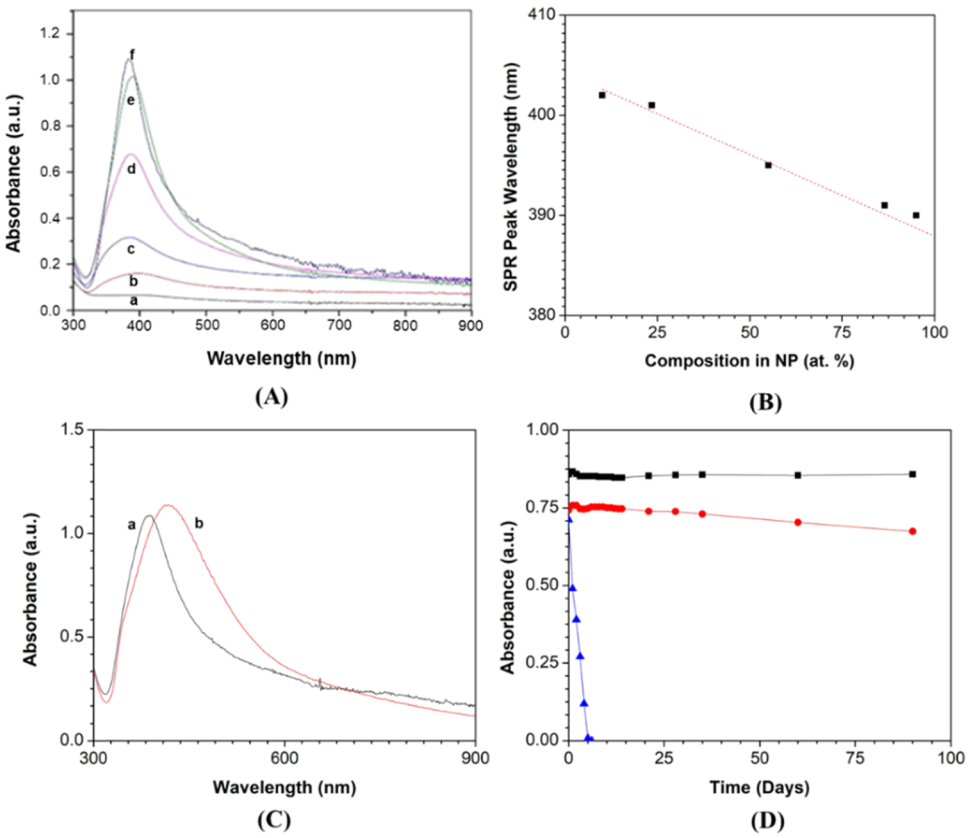

Figure 5. UV−vis spectra for AgCu NPs with different compositions. (A) UV−vis spectra for solution samples of NPs: $Ag_{10}Cu_{90}$ (a, black), $Ag_{23}Cu_{77}$ (b, red), $Ag_{55}Cu_{45}$ (c, blue), $Ag_{86}Cu_{14}$ (d, pink), $Ag_{95}Cu_5$ (e, green), and Ag (f, purple) (150 μL samples diluted in 3 mL of water). (B) Plot of LSPR band position vs the Ag composition in the AgCu NPs (linear regression: $y = -0.163x + 404.2$). (C) UV−vis spectra comparing the $Ag_{86}Cu_{14}$ NPs synthesized under nitrogen (a) and ambient air (b) atmosphere. (D) Plot of SPR band absorbance at 400 nm vs time for $Ag_{86}Cu_{14}$ (a), $Ag_{55}Cu_{45}$ (b), and $Ag_{23}Cu_{77}$ (c) solutions under sealed conditions over a 100-day period.

increased in the NPs. This finding is reminiscent of the surface-mediated Ostwald ripening of AuCu NPs at room temperature.[13] The significance of this finding is that AgCu NPs serve as a new class of room temperature-sinterable NPs for the development of printable nanoinks or nanopastes. The intriguing room temperature-sinterable properties are further characterized by the following DLS and zeta potential analyses.

Figure 3 shows a representative set of DLS plots for the as-synthesized AgCu NPs along with the corresponding zeta potentials. The hydrodynamic particle size and size distribution are shown to increase with Cu% in the NPs (Figure 3A), indicative of the high propensity of aggregation or agglomeration for the high Cu NPs in the solution. The corresponding zeta potentials of the AgCu NPs are negative (Figure 3B), indicative of negative charges on the surface of NPs, which is consistent with citrate being the capping molecule. The charge is shown to decrease with the Cu% in the NPs (Figure 3B), which explains the high propensity of aggregation or agglomeration for the high Cu alloy NPs in the solution as observed by the DLS data (Figure 3A).

Note that agglomeration of NPs could increase the particle size, which is partially responsible for sintering via interparticle coalescence or interparticle necking at room temperature. However, a simple agglomeration process could involve a reversible aggregative process, which does not lead to interparticle coalescence or interparticle necking. As shown by the DLS data, the increase of hydrodynamic diameters reflects mostly such a simple agglomeration process.

Phase Structures. The AgCu NPs of different compositions were further characterized by XRD to determine the phase structures and the grain sizes of the NPs. Figure 4A shows a representative set of XRD patterns. The peak positions fall in between Ag and Cu, indicating that the AgCu NPs feature an fcc nanoalloy characteristic, not a core−shell type structure. This is evidenced by examination of the (111) peak, showing no evidence of phase segregation that would be present in a core−shell structure. This is consistent with lattice shrinking as the Cu% in NPs increases. For example, $Ag_{55}Cu_{45}$ NPs show a single (111) peak, which corresponds to a lattice parameter falling in between the lattice parameter for Ag (0.409 nm) and that for Cu (0.363 nm).[20,21] For NPs with Ag % > 75%, the observation of a separate small (111) shoulder peak (2θ = 37) may be attributed to the presence of a small degree of phase segregation for a different composition.

Based on the XRD data, the lattice parameters of the AgCu NPs of different compositions were obtained (Figure 4B), showing that the lattice parameter increases with the composition of Ag in the NPs. This trend is consistent with that from Vegard's law:

$$LP_{alloy} = xLP_{Ag} + (1 - x)LP_{Cu} \quad (1)$$

where LP_{Ag} and LP_{Cu} are the lattice parameters of pure metals and x is fraction of the components. Subtle differences are evident between the experimental and theoretical values.[22] The good agreement with Vegard's law in terms of the fcc alloy's lattice parameter versus the bimetallic composition serves as a

https://doi.org/10.1021/acs.langmuir.2c00221
Langmuir 2022, 38, 5633−5644

further piece of evidence for the presence of Cu in the as-synthesized AgCu NPs. This result also suggests the presence of additional lattice strain for the NPs with a higher Cu%, which likely reflects the nanoscale effect on the lattice strain.

The average grain size was determined using the Scherrer equation

$$\tau = \frac{k\lambda}{\beta \cos\cos(\theta)} \quad (2)$$

where τ is the mean particle grain size, k is the shape factor, λ is the X-ray wavelength, β is the line broadening at FWHM, and θ is the Bragg angle.[13] The average grain size shows a clear trend of increase with the Ag% composition in the NPs (Figure 4C). This further supports the tendency of sintering for the bimetallic NPs. The average grain size was slightly different from the particle size determined by TEM, reflecting the difference in NP aggregation in the NP samples.

Bimetallic Properties and Stability of NPs. Silver and copper NPs in solutions exhibit strong LSPR bands due to oscillations of surface conduction electrons under an electromagnetic field. These oscillations coincide with specific wavelengths of incident light, which can be identified by UV−vis spectroscopy. The SPR for Ag NPs occurs at a wavelength of 386 nm, while Cu NPs have an expected wavelength of 548 nm.[23] The characterization of the LSPR bands provides information for assessing the composition change and stability of NPs. Figure 5A shows a representative set of UV−vis spectra for AgCu NPs with different compositions. First, the intensity of the LSPR band is shown to decrease with Cu% in the NPs (Figure 5A). Second, the LSPR band is shown to display a subtle red shift to a longer wavelength, along with broadening of the band to the longer wavelength (Figure 5B). The red shift also depends on other factors including a change in the refractive index, particle size, or aggregation. The peak shift reflects a combination of the changes in particle size, size distribution, and metal composition of the AgCu NPs. While there is no apparent red shift of the peak position toward the copper LSPR band with the increase of Cu%, there is peak broadening at the longer wavelength range, indicative of the incorporation of copper in the NPs. The DLS data showed an increase in size as the Cu% in the NPs is increased, likely reflecting the increase in aggregation.

It is evident that increasing the composition of Ag in the bimetallic NPs produced a stronger and sharper absorbance peak at the Ag SPR. This is consistent with the fact that Ag has the strongest SPR band among the coinage metals. As Cu% is increased, the band width widened, and the absorbance decreased. The linear trend of SPR band with the composition (Figure 5B) supports the bimetallic properties of AgCu NPs with controllable bimetallic compositions. Simulation of the LSPR bands of pure AgNPs and pure CuNPs was also performed using the Mie theory for comparison with the experimental UV−vis data (Figure S3 in the Supporting Information). These simulated LSPR bands for AgNPs and CuNPs occur at 386 nm and for Cu at 548 nm, respectively. The LSPR band for pure AgNPs shows a sharp and well-defined peak while CuNPs had a much broader SPR.

The stability of AgCu NPs in solutions was also characterized by monitoring the change of the SPR band. Figure 5C compares the SPR of 1× $Ag_{86}Cu_{14}$ NPs in solutions between the inert and ambient conditions.[24] The solutions were prepared under nitrogen conditions of a Schlenk line to prevent any Cu oxidation and subsequent CuO formation. In comparison, the NPs under ambient atmosphere conditions showed a subtle red shift in the width and SPR position. There are two possibilities for the shift. One possibility is the oxidation of Cu in the NPs due to exposure to O_2. However, there is little change in the peak intensity, which does not seem to support oxidation. It is likely that the NPs under an air atmosphere caused a certain degree of aggregation due to propensity of the surface Cu to undergo partial oxidation and desorption of the capping ligands. This possibility is supported by the observation of aggregation for the NPs synthesized under ambient conditions, which showed a higher degree of aggregation. The long-term stability of the AgCu NPs was monitored by UV−vis spectroscopy over a span of ∼100 days for AgCu NPs of three different compositions (Figure 5D). Each cuvette was kept under N_2 at room temperature. The NPs with a higher Ag% showed much stronger stability than the other NPs. The NPs with higher Ag% are suspendable in the solution apparently due to suppressed formation of CuO, whereas the Cu-rich particles showed a tendency of precipitation due to formation of CuO.[25] The corresponding DLS and zeta potential data for $Ag_{86}Cu_{14}$ and $Ag_{55}Cu_{45}$ NPs in the solutions after more than 100 days (Figure S4) showed relatively little change to the particle size. The slight shift to smaller particle sizes and slightly broader distribution of zeta potential are likely due to subtle differences in the batch-to-batch synthesis. The slightly broader distribution of zeta potentials is likely due to the different synthesis batches.

Room Temperature Sintering Properties. AgCu NPs were formulated into aqueous solution as nanoinks or pastes with a weight percentage of 25% metal NPs and printed onto paper substrates to allow sintering under two different ambient conditions: (1) ambient atmosphere (22 °C, ∼18 RH%) and (2) controlled relative humidity (22 °C, 1−90 RH%).

Sintering under an Ambient Atmosphere. The sheet resistance (Ω/□) was measured using a four-probe multimeter with a 2.0 mm probe spacing. A commercial silver ink/paste was also tested for comparison. Table 1 shows a representative set of results for the sheet resistance values determined after drying the traces printed on the paper substrates under ambient conditions (room temperature). For the 25 wt % $Ag_{86}Cu_{14}$ and $Ag_{55}Cu_{45}$ inks, the sheet resistances are much lower than that from the 100% commercial silver ink by a factor of 110 and 8, respectively. For the $Ag_{23}Cu_{77}$ nanoink, however, the sheet resistance is greater than that of the commercial silver ink by a factor of 60 and is much greater than the AgCu inks with >50% Ag by 2 ∼ 4 of orders of magnitude. The electrical conductivity strongly depends on the bimetallic composition. Using the AgCu nanopaste, conductive tracers and interdigitated devices were printed on paper substrates by screen printing. Figure 6 top panel shows a

Table 1. Comparison of Sheet Resistances for AgCu NPs after Sintering on Photopaper Substrates at Room Temperature (22.5 °C)

composition	sheet resistance (Ω/□)	sintering time (h)
Ag (commercially available)	19.50	22.0
Ag_{100}	1.06	0.55
$Ag_{86}Cu_{14}$	0.17	0.25
$Ag_{55}Cu_{45}$	2.40	0.45
$Ag_{23}Cu_{77}$	1207.60	1.00

https://doi.org/10.1021/acs.langmuir.2c00221
Langmuir 2022, 38, 5633−5644

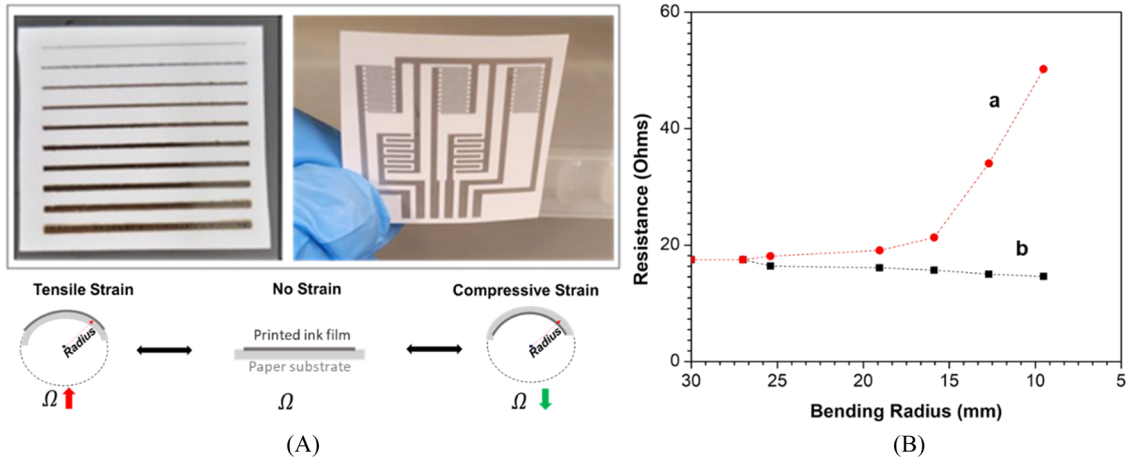

Figure 6. (A) (Top panel) Photos showings conductive traces and interdigitated electrode arrays on a photopaper substrate by screen printing of the $Ag_{55}Cu_{45}$ nanoink (formulated with hydroxyethyl cellulose (30 wt %)). (Bottom panel) Illustration of the device strain test with tensile and compressive strains. (B) Result of the strain test of a 33 mm × 2 mm photopaper strip printed with a conductive $Ag_{55}Cu_{45}$ trace upon tensile (a) and compressive (b) strain.

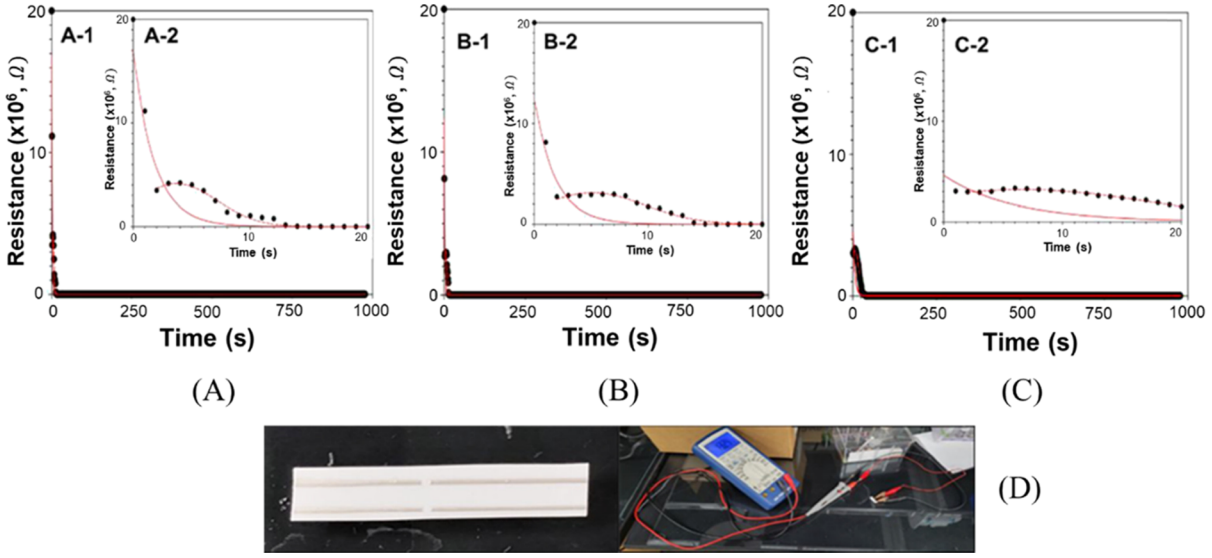

Figure 7. (A–C) Transient changes of the resistances measured following printing the $Ag_{55}Cu_{45}$ (25 wt %) nanoink on the gap area defined by a silver trace on a HP photopaper under ambient conditions. The closed circles in A-1, B-1, and C-1 are the results for sintering of 0.5, 0.5, and 0.75 μL of nanoink dispensed, respectively, where the red lines represent fitting results using eq 3. The A-2, B-2, and C-2 insets are the magnified views of the indicated time region, where the additional red lines represent the fitting results using eq 4. (D) Photo showing the photopaper substrate with conductive silver traces with a 2 mm gap and the electrical measurement setup.

representative set of traces and interdigitated electrode devices on a photopaper substrate prepared by screen printing of $Ag_{55}Cu_{45}$ ink. Each of the printed traces or electrodes is electrically conductive (Table 1) and shows a continuous morphology. The room temperature sintering behavior depends on both the particle size and the binding strength of the capping agent. Based on the analysis of the transient results from the resistance measurements, the irreversible transition to low resistance values indicates the occurrence of NP sintering. Also, based on the XRD comparison between the NPs and the sintered film (Figure S5), the sintered film showed a much larger grain size, indicative of sintering, and a decrease in the lattice parameter, indicative of a higher degree of alloying after sintering. A detailed study of the morphology and structure of the sintered NPs using different imaging and composition analysis techniques will be needed. Based on the previous study on room temperature sintering of AuCu alloy NPs on paper substrates,[13] the complication of the roughness of the porous substrates must be studied via a full assessment of the morphology of the sintered NPs.

The printed AgCu alloy traces on the paper substrate, after ambient sintering, were further examined to assess the device performance upon bending of the paper substrate (Figure 6A, lower panel). Figure 6B shows a representative set of data on the changes of resistance of a 33 mm conductive trace as a function of trace strain in terms of the bending radius of curvature.

For tensile strain (convex), the resistance shows a gradual increase with the reduction of radius of curvature. In contrast, little change was observed for the compressive strain (concave) versus the radius of curvature. This characteristic is desired for the design of a strain sensor.[1]

The room temperature sintering kinetics were also examined by monitoring the resistance of the conductive traces and the

https://doi.org/10.1021/acs.langmuir.2c00221
Langmuir 2022, 38, 5633−5644

interdigitated microelectrodes (IMEs) on the paper substrate immediately following screen printing using a stainless steel 325 micron mesh under ambient conditions. The results are shown in Figure 7A−C, which were measured by printing the $Ag_{55}Cu_{45}$ (25 wt %) nanoink across the 2 mm gap area defined by a silver trace on a paper substrate under ambient conditions and monitoring the change of resistance of the nanoink in the sintering process (Figure 7D). The $Ag_{55}Cu_{45}$ (30 wt %) conductive ink was used in this experiment. Three runs were performed with Run 1 (A) and Run 2 (B) for 0.50 μL of nanoink being dispensed across the 2 mm gap silver trace (R = 0.6Ω) and Run 3 (C) for 0.75 μL of nanoink being dispensed (Figure 7A−C).

For the run with a lower volume of nanoink, the resistance showed a drastic decrease within 50 s down to between 2.00 and 3.50Ω. For the run with a higher volume of nanoink, it took nearly 100 s for the resistance to drastically reduce to a value of 2.00Ω. The change of the resistance (R) can be fitted with a first-order rate kinetic model:

$$R = R_1 + R_2 e^{-kt} \tag{3}$$

where R_1 and R_2 represent the final and initial resistances, respectively, and k is the rate constant for the overall sintering process.

There are two competing processes in sintering. The first is the dominant exponential decay as fitted by the first-order kinetic model (eq 3). The rate constant k clearly depends on the amount of ink applied to the substrate (0.53 and 0.55 s^{-1} for 0.5 μL and 0.17 s^{-1} for 0.75 μL) with the larger quantity showing a smaller rate constant. The average rate constant (k) is 0.54 s^{-1}. The average final resistance (R_1) is 3.7 Ω, and the average initial resistance (R_2) is 1.5 × 10^7 Ω. This process is believed to reflect the aggregation of NPs during the initial drying process, which is accompanied by the growth of the NPs via Ostwald ripening in the surface-mediated sintering process. The second is a process involving an initial resistance increase followed by resistance decrease, which likely reflects a combination of nucleation and growth processes involved in the Ostwald ripening process. For simplicity, we approximate the reaction times by a simple Gaussian distribution in terms of times:

$$R = C_1 \times e^{-0.5\times\left(\frac{t-t_0}{C_2}\right)^2} \tag{4}$$

where C_1 represents the peak height (maximum resistance) and C_2 corresponds to half width of the peak at about 60% of the peak height and t_0 represents the peak position (the time taken to reach the maximum resistance). The fitting parameters with these two kinetic equations (eqs 3 and 4) are shown below in Table 2. The average peaking time (t_0) is 4 s with an average half width of the time distribution of 4.4 s. The average maximum peak resistance is 3.45 × 10^6 Ω. The values of the fitting parameters strongly depend on the volume of the nanoink dispensed on the substrates. When more ink is deposited on the substrate, the kinetics follow a slower process, reflecting the dissolution of small particles via Ostwald ripening, which is reminiscent of the observation of resistance peaking for the AuCu NP sintering process.[14] In the sintering process, there is a transition from the not fully continuous film (less conductive state) of the sintered domains to a continuous film with the interconnected NPs (more conductive state).

The thickness of the nanoink-printed trace was also controlled by controlling the amount of nanoink deposited on the paper substrate. As shown in Figure S6, the measured sheet resistance is shown to strongly depend on the thickness of the nanoink-printed trace, which was controlled by dispensing 0.5 μL of $Ag_{86}Cu_{14}$ (30 wt %) to produce a 1 cm trace in successive layers. The thickness of the traces ranged from 10 to 48 μm. The resistivity of the traces decreases with thickness, indicating likely the important role of interparticle sintering in addition to surface-mediated sintering. Additional paper substrates were also tested with this nanoink, including cellulose nanofibrous substrates, standard 8G letter paper, and Whatman filter paper (#1), where the sintered film on the HP paper showed the lowest resistance. However, a detailed assessment of the substrate dependence remains to be studied in future work.

Table 2. Fitting Results from Fitting the Transient Changes of the Resistances in Figure 7

fitting parameters							
eq 3				eq 4			
volume of ink (μL)	R_1 (Ω)	R_2 (Ω)	k (s^{-1})	volume of ink (μL)	C_1 (Ω)	C_2 (s)	t_0 (s)
0.50	4.2	1.7 × 10^7	0.55	0.50	4.2 × 10^6	3.70	3.40
0.50	3.1	1.2 × 10^7	0.53	0.50	2.7 × 10^6	5.10	4.60
0.75	3.4	4.6 × 10^7	0.17	0.75	3.1 × 10^6	6.70	11.0

Sintering under Controlled Relative Humidity. Given the operation of both interparticle sintering and surface-mediated sintering in the ambient sintering process, we further monitored the sintering process under controlled relative humidity. This experiment is performed by printing a nanoink onto a screen-printed silver IME, which is then sintered under ambient conditions. This device is then exposed to a chamber with controlled humidity at room temperature and concurrent measurement of the resistance is performed.

Figure 8 bottom panel shows a representative set of transient changes of the resistance values of the AgCu nanoinks under controlled relative humidity. With a nanoink of $Ag_{55}Cu_{45}$ (30 wt %) printed on a screen-printed silver IME, upon drying under ambient conditions, the film has a very low two-probe resistance value (8 Ω). This film shows no change upon exposure to 50% RH (Figure 8 bottom panel A), indicating no effect of water vapor on the fully sintered film. In contrast, with a nanoink of $Ag_{55}Cu_{45}$−hydroxyethyl cellulose (HEC) (30−30 wt %) printed on the screen-printed silver IME, upon drying under ambient conditions, the film has a high two-probe resistance value (7.00 MΩ) and shows a remarkable reduction of the resistance upon exposing to a controlled humidity of 40%RH at room temperature (Figure 8 bottom panel B). Upon exposure to 40%RH, the resistance shows a rapid decrease from 7 MΩ to a value of 6.81 Ω. This value remains until switching from 40 to 2%RH under N_2. When successive cycles are carried out between 40%RH and 2%RH for 2000 s, the resistance is stabilized at 9.11 Ω. We believe that this is the first example demonstrating the water vapor-induced sintering of AgCu NPs with a cellulose additive in the nanoink at room temperature. Note that sintering is an irreversible process. When there is no sintering, a reversible change in resistance would signify a change in interparticle distance only. When sintering occurs, the change is irreversible. In the presence of HEC in the ink formulation, NPs could not fully sinter initially, but the water effectively dilutes the concentration of HEC in

https://doi.org/10.1021/acs.langmuir.2c00221
Langmuir 2022, 38, 5633−5644

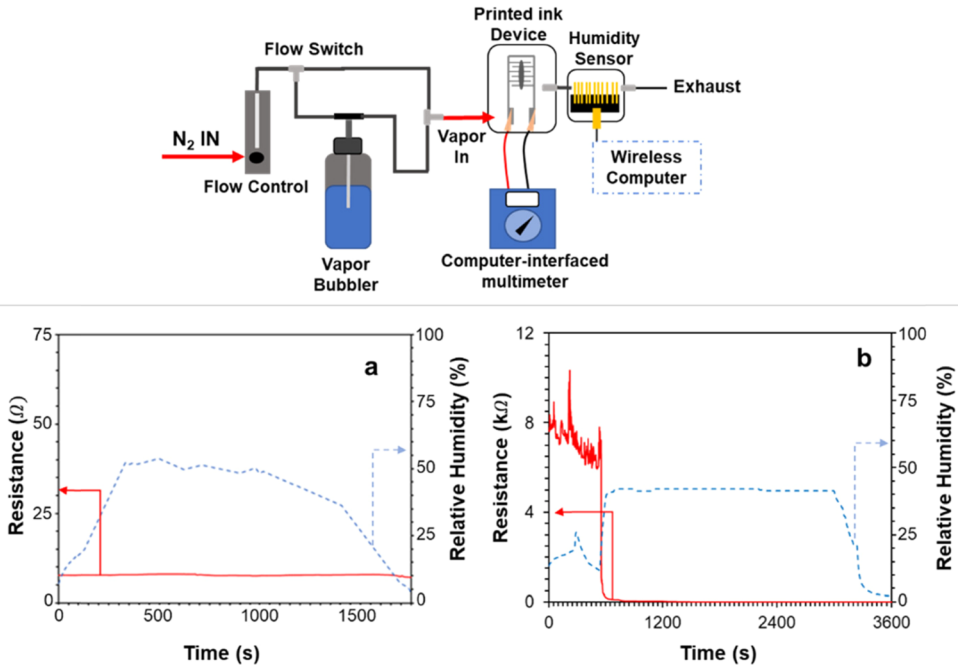

Figure 8. (Top Panel) A scheme showing the measurement setup. Bottom panel (a,b): transient curves showing the changes of resistance of the nanoink-printed IME device with a film of (a) $Ag_{55}Cu_{45}$(30 wt %) and (b) $Ag_{55}Cu_{45}$–HEC (30–30 wt %).

the NP film and changes the surface tension, leading to effective sintering.

We have examined the humidity-regulated sintering of AgCu nanoinks with different formulations on IME devices, including bimetallic compositions and cellulose additives ($Ag_{86}Cu_{14}$, $Ag_{86}Cu_{14}$–HEC, $Ag_{23}Cu_{77}$, and $Ag_{23}Cu_{77}$–HEC). Figure S7 shows a representative set of data for $Ag_{86}Cu_{14}$ and $Ag_{86}Cu_{14}$–HEC. For $Ag_{86}Cu_{14}$, the initial low resistance of the film is indicative of the film being fully sintered on the substrate before the water vapor treatment is introduced. Upon exposure to water vapor, there is no response in the resistance. For $Ag_{86}Cu_{14}$–HEC (30 wt %:30 wt %) also, there is no response to humidity, indicative of a film that is already sintered, which is in stark contrast to the $Ag_{55}Cu_{45}$ HEC (30 wt %:30 wt %) conductive films. The $Ag_{86}Cu_{14}$ alloy inks with and without HEC are capable of room temperature sintering without the presence of water vapor. Figure S8 shows a representative set of data for $Ag_{23}Cu_{77}$ and $Ag_{23}Cu_{77}$–HEC. For $Ag_{23}Cu_{77}$, there is a dramatic negative response to the increase in humidity, in sharp contrast to the $Ag_{86}Cu_{14}$ film. As the humidity increases, the resistance reduces by 4 orders of magnitude, and interestingly, it shows a return to the original high resistance upon purging with nitrogen (Figure S8A). For $Ag_{23}Cu_{77}$ HEC (30 wt %:30 wt %) also, there is a dramatic negative response to the increase in humidity (Figure S8B), similar to the $Ag_{55}Cu_{45}$ film. The unsintered $Ag_{23}Cu_{77}$ NPs in a dry state did not undergo sintering even in the presence of water vapor. Instead, they underwent reversible changes in interparticle distances and dielectric medium properties, where the HEC additive regulates the adsorption of water vapor in the film. While surface-mediated interconnection is believed to be responsible for the initial sintering of the nanoink on the paper substrate along with a limited degree of interparticle sintering under ambient conditions, a water vapor-assisted interparticle necking is likely to play a role in the drastic reduction of the resistance. In this mechanism, the adsorption of cellulose in the film may have increased the surface tension of the NPs, allowing it to sinter at a faster time at room temperature. The mechanistic details of this phenomenon will be discussed in the next subsection.

Theoretical Simulation of Sintering. Based on the recent theoretical simulations on sintering of Ag and Cu NPs, nanoscale Ag and Cu NPs were shown to undergo near-room temperature sintering toward bulk conductivity. The adsorption energies of Ag or Cu atom on the surface depend on $E_{\text{Ag or Cu}}$, $E_{\text{cellulous surface}}$, and $E_{\text{atom/metal surface}}$, which are the total energies for the isolated Ag or Cu atom, the isolated substrate (e.g., cellulose), and Ag or Cu atom adsorption on metal surfaces, respectively. The activation energy of diffusion (E_{diff}) is the barrier of the diffusion that was calculated by $\Delta E_a = E_{TS} - E_{IS}$, where the energies of the transition state (E_{TS}) and the initial state (E_{IS}) were obtained with ZPE corrections.[13,26] Theoretical simulations of the sintering processes were carried out in terms of the surface-mediated Ostwald ripening process using the Gibbs–Thompson (GT) model coupled with the modified bond additivity (MBA) model by considering the atom mobilities of the different metals on the surface:[29]

$$\frac{dR}{dt} = \frac{K}{R}\left(e^{-E_{tot}/kT}\right)\left(e^{2\gamma\Omega/kTR^*} - e^{2\gamma\Omega/kTR}\right) \quad (5)$$

where R is the radius of a nanoparticle, t is time, E_{tot} is the total energy, k is the Boltzmann constant, T is temperature, γ is the surface free energy, and Ω is the atomic volume of the bulk metal. R^* represents the critical nanoparticle size at which the size neither increases or decreases. K is expressed as $K = (2\sin\theta)\, V_p\, \Omega/a(2 - 3\cos\theta + (\cos\theta)^3)$, where θ is the contact angle, a is the interatomic distance, and V_p is the frequency of thermal vibration of atoms. The total energy (E_{tot}) is expressed as

$$E_{tot} = (\Delta H_{sub} - (E_{ads}^{\ support} - E_{diff}^{\ support}) \quad (6)$$

https://doi.org/10.1021/acs.langmuir.2c00221
Langmuir 2022, 38, 5633–5644

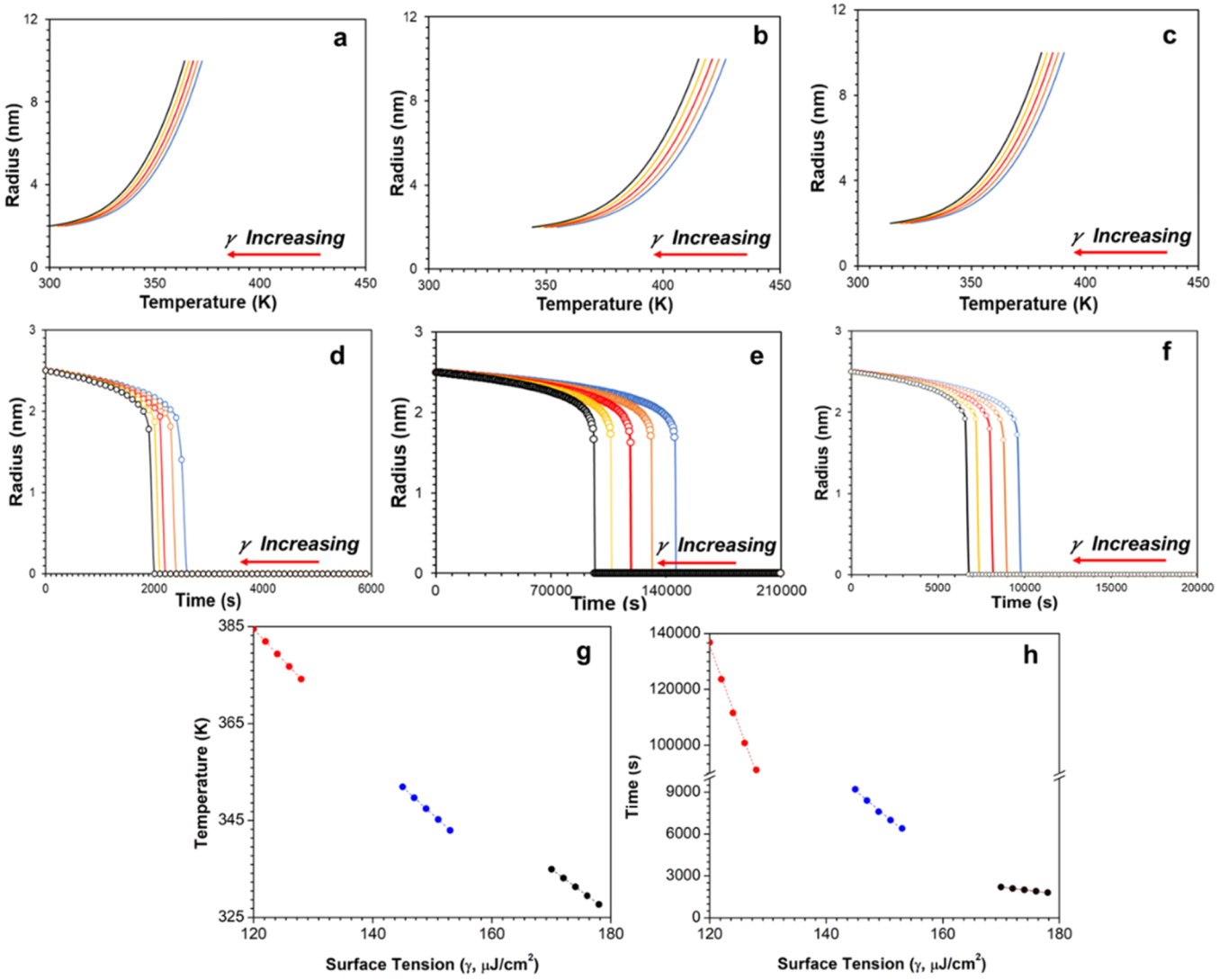

Figure 9. Simulation results based on the GT model for the sintering processes of Cu, Ag, and AgCu NPs. (a–c): temperature dependence of the growth of the larger NPs for (a) Cu, (b) Ag, and (c) AgCu (50:50) at different surface tensions; (d–f): kinetics for the disappearance of the smaller particles for (d) Cu, (e) Ag, and (f) AgCu (50:50) at different surface tensions (Cu: 140, 142, 144, 146, and 148 μJ/cm^2; Ag: 120, 122, 124, 126, and 128 μJ/cm^2; and AgCu: 145, 147, 149, 151, and 153 μJ/cm^2). (g–h): Plots of temperature corresponding to the grown large particles at 1 nm vs surface tension (data from panels (d–f)) (g) and time corresponding to the disappearing small particles at 0.5 nm vs surface tension increases (data from panels (a–c)) (h).

where ΔH_{sub} is the sublimation energy, $E_{ads}^{support}$ is the adsorption energy of a metal atom on the substrate surface, and $E_{diff}^{support}$ is the activation energy for the diffusion of a metal atom on the substrate surface. To determine a more accurate total energy, we also considered the nanoparticle size effect on sublimation energy,[27] which is expressed as $\Delta H_{sub}(R) = \Delta H_{sub}^{\infty} - 2\varepsilon_s M/\rho R$, where $\Delta H_{sub}(R)$ is the sublimation energy at a specific size, ΔH_{sub}^{∞} is the sublimation energy of a bulk solid metal, ρ is the bulk solid-phase density, and M is the molar mass. ε_s is the specific surface energy[28] expressed as $\varepsilon_s(R) = (1 - 2\delta/R + A/R^2)\varepsilon_s$, where δ is the Tolman length with a value of 0.3∼0.6, A ($=2\pi RL$) is area, and ε_s is the specific surface energy of a bulk solid. The understanding of the findings is aided by examining how adhesion, mobility, and surface free energy of the two types of atoms play a role in the sintering process. Theoretically, the surface-mediated Ostwald ripening (OR) based on the GT model coupled with the MBA model includes parameters such as sublimation energy (ΔH_{sub}), adsorption energy (E_{ads}), and activation energy for diffusion (E_{diff})) of metal atoms on the surface, which provides a good assessment of the sintering process. Using typical values found for bulk metals, the simulated size evolution for Ag and Cu showed no indication of sintering near room temperature.[13]

With the literature-available bulk and nanoscale parameters for Ag and Cu (Table S1), we simulated the sintering kinetics. With the calculated size-dependent ΔH_{sub} and cellulose surface-mediated E_{ads} and E_{diff}, the surface-mediated E_{tot} was considered in the GT–MBA simulation. We obtained E_{tot} = 300.45 and 290.7 kJ/mol for bulk Ag and Cu, respectively. Figure 9a,b and d,e show a set of simulation results for Cu and Ag in terms of time for the temperature dependence of the growth of the large particles and the kinetics for the disappearance of small particles. With the typical values of surface tension of 140 μJ/cm^2 for Cu and 120 μJ/cm^2 for Ag, the results show that the growth of Cu and Ag particles occurs at temperatures very close to room temperature. The sintering temperature for Cu is much lower than that for Ag. The higher

https://doi.org/10.1021/acs.langmuir.2c00221
Langmuir 2022, 38, 5633–5644

surface free energy and lower sublimation enthalpy would result in a lower sintering temperature, which is consistent with our earlier findings for AuCu alloy NPs.[13] We also simulated the sintering process for AgCu (50:50) by assuming average values for some of the sintering parameters, for example, 145 μJ/cm^2 for the surface tension (Table S1), and the results are shown in Figure 9c,f. The sintering kinetics and temperatures are found to fall in between Cu and Ag.

Based on Young's equation for surface tensions (γ, surface free energy) vs contact angle (θ):

$$\gamma_{(\text{metal}-\text{liquid})} = \gamma_{(\text{metal})} - \gamma_{(\text{liquid})} \cos(\theta) \quad (7)$$

where we estimate the relative change of the Ag/HEC solution interfacial surface tension upon adsorption of water in the nanoink film. Consider that the change of contact angle (θ) for the HEC-containing water layer on Ag NPs would fall in between 0 and 90 degrees depending on the concentration of HEC. The surface free energy of water is 7.3 μJ/cm^2. The change of $\gamma_{(\text{Ag}-\text{water})}$ of Ag under water is thus expected to fall in between 0 and 7.3 ($\gamma_{(\text{Ag}-\text{water})} = \gamma_{(\text{Ag})} - \gamma_{(\text{water})} \cos(\theta)$).[30] By increasing the surface free energy accordingly for Ag (120, 122, 124, 126, and 128 μJ/cm^2)[30] and Cu (170, 172, 174, 176, and 178 μJ/cm^2),[31] the simulations yield the results shown in Figure 9g,h. The results, indeed, indicate that the sintering time decreases for the disappearance of smaller Ag and Cu NPs (a,b) and the sintering temperature decreases for the growth of larger Ag and Cu NPs (d,e). By further considering that the surface free energy of the AgCu alloy can be approximated as an average of those of Ag and Cu based on a recent study,[32] that is, 145 μJ/cm^2 from the average of 120 and 170 μJ/cm^2, the results (Figure 9c,f) show the disappearance of smaller AgCu NPs (c) and sintering temperature decrease for the growth of larger AgCu NPs.

The surface free energy changes clearly play an important role in the sintering process as demonstrated by the GT model simulation results above. It is likely that the surface free energy of the NPs changes upon adsorption of water vapor in the nanoink-printed film. The surface free energy of the metal NPs is expected to increase upon adsorption of water containing HEC on the surface. This is supported by a recent study of the surface free energy change as a function of the concentration of HEC on Si wafer surfaces[32] in which the surface free energy is shown to increase with the decrease of HEC in aqueous solution. Under an elevated RH% in the atmosphere, the adsorption of water would effectively dilute the concentration of HEC near the particle surface, thus leading to the increase of the surface free energy. This results in a decrease of the sintering time. The sintering temperature is also shown to drastically reduce. This offers one likely reason to explain the accelerated sintering of AgCu NPs with the HEC additive in the ink formulation upon adsorption of water vapor. The hydrophilic HEC additive facilitates the adsorption of water vapor to increase the surface tension, favoring interparticle necking as a sintering mechanism.

CONCLUSIONS

We have developed a scalable wet chemical synthesis route for AgCu alloy NPs with controllable bimetallic compositions and room temperature sintering capability. The bimetallic alloy structure and morphology as well as the nanoparticle stability were characterized by determining the LSPR of the nanoparticle, the alloy structure, and the particle size and zeta potential. The bimetallic alloy nanoinks have been demonstrated to be stable in controlled ink formulations and sinterable under room temperature. In addition to composition dependence, the results reveal an intriguing dependence of sintering on humidity above the printed nanoink films. The NPs are formulated as inks/pastes for printable applications with a high degree of conductivity. These findings are assessed based on theoretical simulation of the sintering process in terms of a combination of surface-mediated sintering and interparticle necking mechanisms, nanoscale adsorption, adhesion, and diffusion, and the surface free energies of the NPs. The bimetallic alloy nanoinks, depending on the composition, displayed a relatively high degree of stability and scalability. The alloy NPs can be formulated into conductive inks and pastes, and the room temperature sintering capabilities may find use in a wide range of applications in printable electronics and wearable sensors. In addition to refining the synthesis parameters for a better control of the nanoparticle size,[33] an in-depth study of the factors controlling the room temperature sintering process, along with the understanding of the interaction between the NPs and the substrate, is part of our further investigations in the development of commercially viable conductive inks and pastes.

ASSOCIATED CONTENT

Supporting Information

The Supporting Information is available free of charge at https://pubs.acs.org/doi/10.1021/acs.langmuir.2c00221.

Additional experimental details, characterization results, and simulation results (PDF)

AUTHOR INFORMATION

Corresponding Author

Chuan-Jian Zhong − *Department of Chemistry, State University of New York at Binghamton, Binghamton, New York 13902, United States;* orcid.org/0000-0003-0746-250X; Email: cjzhong@binghamton.edu

Authors

Richard Robinson − *Department of Chemistry, State University of New York at Binghamton, Binghamton, New York 13902, United States*

Virginia Krause − *Department of Chemistry, State University of New York at Binghamton, Binghamton, New York 13902, United States*

Shan Wang − *Department of Chemistry, State University of New York at Binghamton, Binghamton, New York 13902, United States*

Shan Yan − *Department of Chemistry, State University of New York at Binghamton, Binghamton, New York 13902, United States*

Guojun Shang − *Department of Chemistry, State University of New York at Binghamton, Binghamton, New York 13902, United States*

Justine Gordon − *Department of Chemistry, State University of New York at Binghamton, Binghamton, New York 13902, United States*

Serena Tycko − *Department of Chemistry, State University of New York at Binghamton, Binghamton, New York 13902, United States*

Complete contact information is available at:

https://doi.org/10.1021/acs.langmuir.2c00221
Langmuir 2022, 38, 5633−5644

https://pubs.acs.org/10.1021/acs.langmuir.2c00221

Notes

The authors declare no competing financial interest.

■ ACKNOWLEDGMENTS

This work was supported by the National Science Foundation (CHE 2102482 AND IIP 1923323). The authors thank Mr. D. Collins for his assistance in ICP−OES analysis, Prof. D. Jenkins for his assistance with XRD characterization, and Prof. H. Guo for her assistance in DLS characterization.

■ REFERENCES

(1) Wu, Z.; Shan, S.; Zang, S.; Zhong, C. Dynamic core−shell and alloy structures of multimetallic nanomaterials and their catalytic synergies. *Acc. Chem. Res.* **2020**, *53*, 2913−2924.

(2) Heuer-Jungemann, A.; Feliu, N.; Bakaimi, I.; Hamaly, M.; Alkilany, A.; Chakraborty, I.; Masood, A.; Casula, M.; Kostopoulou, A.; Oh, E.; Susumu, K.; Stewart, M.; Medintz, I.; Stratakis, E.; Parak, W.; Kanaras, A. The Role of Ligands in the Chemical Synthesis and Applications of Inorganic Nanoparticles. *Chem. Rev.* **2019**, *119*, 4819−4880.

(3) Njoki, P.; Luo, J.; Kamundi, M.; Lim, S.; Zhong, C. Aggregative growth in the size-controlled growth of monodispersed gold nanoparticles. *Langmuir* **2010**, *26*, 13622−13629.

(4) Xu, G.; Chen, Y.; Tazawa, M.; Jin, P. Surface Plasmon Resonance of Silver Nanoparticles on Vanadium Dioxide. *J. Phys. Chem. B* **2006**, *110*, 2051−2056.

(5) Masson, J. F. Portable and field-deployed surface plasmon resonance and plasmonic sensors. *Analyst* **2020**, *145*, 3776−3800.

(6) Cheng, H.; Yan, S.; Shang, G.; Wang, S.; Zhong, C. Strain sensors fabricated by surface assembly of nanoparticles. *Biosens. Bioelectron.* **2021**, *186*, No. 113268.

(7) Zeng, S.; Shan, S.; Lu, A.; Wang, S.; Caracciolo, D.; Robinson, R.; Shang, G.; Xue, L.; Zhao, Y.; Zhang, A.; Liu, Y.; Liu, S.; Liu, Z.; Bai, F.; Wu, J.; Wang, H.; Zhong, C. Copper-Alloy Catalysts: Structural Characterization and Catalytic Synergies. *Catal. Sci. Technol.* **2021**, *11*, 5712−5733.

(8) Tang, L.; Zhu, L.; Tang, F.; Yao, C.; Wang, J.; Li, L. Mild Synthesis of Copper Nanoparticles with Enhanced Oxidative Stability and Their Application in Antibacterial Films. *Langmuir* **2018**, *34*, 14570−14576.

(9) Sharma, G.; Kumar, A.; Sharma, S.; Naushad, M.; Prakash Dwivedi, R.; Al Othman, Z. A.; Mola, G. T. Novel development of nanoparticles to bimetallic nanoparticles and their composites: A review. *J. King Saud Univ., Sci.* **2019**, *31*, 257−269.

(10) Harai, M.; Kumar, A. Wavelength tuning of surface plasmon resonance by annealing silver-copper nanoparticles. *J. Appl. Phys.* **2006**, *100*, No. 014309.

(11) Pang, J.; Xie, R.; Chua, S.; Zou, Y.; Tang, M.; Zhang, F.; Chai, F. Preparation of fluorescent bimetallic silver/copper nanoparticles and their utility of dual-mode fluorimetric and colorimetric probe for Hg^{2+}. *Spectrochim. Acta A* **2021**, *261*, No. 120035.

(12) Li, C.; Yao, Y. Synthesis of bimetallic core-shell silver-copper nanoparticles decorated on reduced graphene oxide with enhanced electrocatalytic performance. *Chem. Phys. Lett.* **2020**, *761*, No. 137726.

(13) Yan, S.; Shan, S.; Wen, J.; Li, J.; Kang, N.; Wu, Z.; Lombardi, J.; Cheng, H.; Wang, J.; Luo, J.; He, N.; Mott, D.; Wang, L.; Ge, Q.; Hsiao, B. S.; Poliks, M.; Zhong, C. Surface-Mediated Interconnections of Nanoparticles in Cellulosic Fibrous Materials toward 3D Sensors. *Adv. Mater.* **2020**, *32*, No. 2002171.

(14) Zhao, W.; Rovere, T.; Weerawarne, D.; Osterhoudt, G.; Kang, N.; Joseph, P.; Luo, J.; Shim, B.; Poliks, M.; Zhong, C. Nanoalloy Printed and Pulse-Laser Sintered Flexible Sensor Devices with Enhanced Stability and Materials Compatibility. *ACS Nano* **2015**, *9*, 6168−6177.

(15) Yin, J.; Shan, S.; Yang, L.; Mott, D.; Malis, O.; Petkov, V.; Cai, F.; Shan Ng, M.; Luo, J.; Chen, B. H.; Engelhard, M.; Zhong, C. Gold−Copper Nanoparticles: Nanostructural Evolution and Bifunctional Catalytic Sites. *Chem. Mater.* **2012**, *24*, 4662−4674.

(16) Rezaga, B. F. Y.; Balela, M. D. L. Chemical Sintering of Ag Nanoparticle Conductive Inks at Room Temperature for Printable Electronics. *J. Mater. Sci.: Mater. Electron.* **2021**, *32*, 17764−17779.

(17) Peng, P.; Li, L.; Guo, W.; Hui, Z.; Fu, J.; Jin, C.; Liu, Y.; Zhu, Y. Room-temperature Joining of Silver Nanoparticles Using Potassium Chloride Solution for Flexible Electrode Application. *J. Phys. Chem. C* **2018**, *122*, 2704−2711.

(18) Dai, X.; Xu, W.; Zhang, T.; Shi, H.; Wang, T. Room temperature sintering of Cu-Ag core-shell nanoparticles conductive inks for printed electronics. *Chem. Eng. J.* **2019**, *364*, 310−319.

(19) Okada, S.; Nakahara, Y.; Watanabe, M.; Tamai, T.; Kobayashi, Y.; Yajima, S. Room-Temperature Coalescence of Tri-n-Octylphosphine-Oxide-Capped Cu-Ag Core-Shell Nanoparticles: Effect of Sintering Agent and/or Reducing Agent. *Bull. Chem. Soc. Jpn.* **2021**, *94*, 1616−1624.

(20) Mehtab, S.; Zaidi, M. G. H.; Irshad, T. Designing Fructose Stabilized Silver Nanoparticles for Mercury(II) Detection and Potential Antibacterial Agents. *Mater. Sci. Res. India* **2018**, *15*, 241−249.

(21) Wu, Z.; Shan, S.; Xie, Z.; Kang, N.; Park, K.; Hopkins, E.; Yan, S.; Sharma, A.; Luo, J.; Wang, J.; Petkov, V.; Wang, L.; Zhong, C. Revealing the Role of Phase Structures of Bimetallic Nanocatalysts in the Oxygen Reduction Reaction. *ACS Catal.* **2018**, *8*, 11302−11313.

(22) Denton, A.; Ashcroft, N. Vegard's law. *Phys. Rev. A* **1991**, *43*, 3161−3164.

(23) Kafle, B. P. Introduction to nanomaterials and application of UV−Visible spectroscopy for their characterization. Chapter 6 In *Chemical Analysis and Material Characterizationby Spectrophotometry*; Elsevier Science, 2019; pp 147−198.

(24) Gorham, J. M.; Rohlfing, A. B.; Lippa, K. A.; MacCuspie, R. I.; Hemmati, A.; David Holbrook, R. Storage Wars: how citrate-capped silver nanoparticle suspensions are affected by not-so-trivial decisions. *J. Nanopart. Res.* **2014**, *16*, 14.

(25) Kumar, B.; Smita, K.; Cumbal, L.; Debut, A.; Angulo, Y. Biofabrication of copper oxide nanoparticles using Andean blackberry (*Rubus glaucus* Benth.) fruit and leaf. *J. Saudi Chem. Soc.* **2017**, *21*, S475−S480.

(26) Regel, A.; Glazov, V. Changes in Entropy Semiconductor Electron Subsystem on Fusion. In *Physics of Disordered Materials*, Adler, D., Fritzshe, H., Ovshinsky, S., Eds.; Springer Publishing, 1985; pp 275−285

(27) Campbell, C.; Parker, S.; Starr, D. The effect of size-dependent nanoparticle energetics on catalyst sintering. *Science* **2002**, *298*, 811−814.

(28) Aqra, F.; Ayyad, A. Surface free energy of alkali and transition metal nanoparticles. *Appl. Surf. Sci.* **2014**, *314*, 308−313.

(29) Brillo, J.; Lauletta, G.; Vaianella, L.; Arato, E.; Giuranno, D.; Novakovic, R.; Ricci, E. Surface Tension of Liquid Ag−Cu Binary Alloys. *ISIJ Int.* **2014**, *54*, 2115−2119.

(30) Samsonov, V.; Chernyshova, A. On the Dependence of Surface Tension of Liquids on the Curvature of the Liquid−Vapor Interface. *Colloid J.* **2016**, *78*, 378385.

(31) Jia, M.; Lai, Y.; Tian, Z.; Liu, Y. Calculation of the surface free energy of fcc copper nanoparticles. *Modell. Simul. Mater. Sci. Eng.* **2008**, *17*, No. 015006.

(32) Tsuchiya, K.; Mori, Y.; Kawaguchi, M. Effects of Hydroxyethyl Cellulose and Colloidal Silica Abrasive on the Hydrophilicity of Polished Si Wafer Surfaces. *ECS J. Solid State Sci. Technol.* **2017**, *6*, P361.

(33) Gawande, M. B.; Goswami, A.; Felpin, F.-X.; Asefa, T.; Huang, X.; Silva, R.; Zou, X.; Zboril, R.; Varma, R. S. Cu and Cu-Based Nanoparticles: Synthesis and Applications in Catalysis. *Chem. Rev.* **2016**, *116*, 3722−3811.